

Stabilizing Zinc Electrodeposition in a Battery Anode by Controlling Crystal Growth

Shuo Jin, Duhan Zhang, Arpita Sharma, Qing Zhao, Yiqi Shao, Pengyu Chen, Jingxu Zheng, Jiefu Yin, Yue Deng, Prayag Biswal, and Lynden A. Archer*

Reversible electrodeposition of metals at liquid-solid interfaces is a requirement for long cycle life in rechargeable batteries that utilize metals as anodes. The process has been studied extensively from the perspective of the electrochemical transformations that impact reversibility, however, the fundamental challenges associated with maintaining morphological control when a intrinsically crystalline solid metal phase emerges from an electrolyte solution have been less studied, but provide important opportunities for progress. A crystal growth stabilization method to reshape the initial growth and orientation of crystalline metal electrodeposits is proposed here. The method takes advantage of polymer-salt complexes (PEG-Zn²⁺-aX⁻) (a = 1,2,3) formed spontaneously in aqueous electrolytes containing zinc (Zn²⁺) and halide (X⁻) ions to regulate electro-crystallization of Zn. It is shown that when X = Iodine (I), the complexes facilitate electrodeposition of Zn in a hexagonal closest packed morphology with preferential orientation of the (002) plane parallel to the electrode surface. This facilitates exceptional morphological control of Zn electrodeposition at planar substrates and leads to high anode reversibility and unprecedented cycle life. Preliminary studies of the practical benefits of the approach are demonstrated in Zn-I2 full battery cells, designed in both coin cell and single-flow battery cell configurations.

underlying complexity of the ion desolvation and crystallization processes that ultimately yields a solid metal phase, from electroreduction of solvated ions in a liquid electrolyte medium.^[1] This aspect of electrodeposition is always important but is not emphasized in conventional studies of the process as a scalable method for manufacturing thin coatings of metals,^[2] colloids,^[3] and polymer^[4] on electronically conductive substrates. The strong revival of interest in rechargeable batteries that employ metals as anodes, including lithium (Li), sodium (Na), potassium (K), magnesium (Mg), calcium (Ca), zinc (Zn), and aluminum (Al),^[5–8] which are all crystalline solid materials with unique crystal structures and well-known to electrodeposit in morphologies that often have no relationship to the orientation or structure of the substrate, underscores the need for improved understanding and regulation of crystal growth during metal electrodeposition processes.

1. Introduction


Electrodeposition of metals has been studied extensively from an electrochemistry perspective. The fundamental simplicity of the electrode reaction ($M^{z+} + ze^- \rightleftharpoons M$) belies the

A body of work already exists that shows that regulation of crystal structure can play an important role in the metal electrodeposition morphology. Among these studies, the recent contribution by Zheng et al.,^[6] stands out because it shows that aligned graphene or Au interfacial layers strongly influence the crystal orientation and coating morphology formed by electrodeposited Zn and Au, respectively. Significantly, in the case of the graphene-Zn system, there is evidence that a textured graphene layer can template Zn crystal growth well into the electrodeposited metal bulk, yielding Zn electrodes with unprecedented, high levels of reversibility in simple ZnSO₄ aqueous electrolytes. The present study is also inspired by recent works showing that primarily (110) textured Li electrodeposits are formed in some electrolytes^[9] (e.g., 1 M LiTFSI + 1% LiNO₃ in DOL/ DME and 5 M S₈ +1 M LiTFSI+1% LiNO₃ in DOL/DME, etc), but not in others. These findings suggest that unregulated crystal growth processes at metal anodes must be understood and managed in order to achieve the high levels of morphological control needed for electrochemical cells based on metal anodes to achieve levels of long-term performance relevant for practical applications. Consequences of poor control of metal electrodeposit morphology at a battery anode has been reviewed extensively during the last decade,^[10,11] and it is now known that failure to control morphology at a metal anode

S. Jin, A. Sharma, Dr. Q. Zhao, Y. Shao, P. Chen, Dr. J. Yin, Dr. P. Biswal, Prof. L. A. Archer
Robert Frederick Smith School of Chemical and Biomolecular Engineering
Cornell University
Ithaca, NY 14853, USA
E-mail: laa25@cornell.edu

Dr. D. Zhang
Department of Mechanical and Aerospace Engineering
Cornell University
Ithaca, NY 14853, USA

Dr. J. Zheng, Y. Deng
Department of Materials Science and Engineering
Cornell University
Ithaca, NY 14853, USA

 The ORCID identification number(s) for the author(s) of this article can be found under <https://doi.org/10.1002/sml.202101798>.

DOI: 10.1002/sml.202101798

during charging leads to a long list of problems, all of which leads to poor reversibility and premature failure of the battery anode. The list includes: 1) concentration of electric field lines at irregular deposit features (e.g., bumps, edges, etc.) to drive nonplanar electrodeposition growth in the form of diffusion-limited, dendritic structures^[12,13] which may bridge the inter-electrode space and cause short-circuit the battery; 2) uneven metal deposition during the charge cycle leads to uneven electro-winning during the discharge, producing undesirable effects such as orphaning, when the metal deposit breaks away from the substrate and therefore becomes electrochemically inaccessible.^[14–16] This process has been shown by means of operando optical visualization studies in sodium batteries to drive large decreases in Coulombic efficiency (CE) in battery cycling.^[17]

The use of salt and molecular additives for controlling growth of desired crystalline facets and shape of crystalline nanomaterials is a well-developed concept in materials synthesis.^[18–21] For example, salts, surfactants, and polymers are routinely used in hydrothermal synthesis to induce and/or block certain crystal planes to reform the crystal growth structure.^[18] Selective growth of (111) oriented triangular/truncated triangular particles of Au, Pt, Ag, etc. have been shown to be enabled by halide ions in solution.^[18,19] The ions are believed to regulate growth by selectively adsorbing on some facets,^[20] such as at the (111) plane of Au, Pt, and (002) plane of Zn. We hypothesize that similar approaches could be used to regulate metal crystallization and for controlling morphology of metal electrodes in electrochemical cells. Specifically, we propose that integration of inhibitors with fast adsorption kinetics to specific crystal facets can be used to selectively regulate crystal growth. If crystal growth on planes parallel to the electrode substrate is selectively slowed, for instance, (110) plane of Li and Cu, (002) plane of Zn and Ti, and (111) plane of Au and Ag, it should be possible to drive anisotropic, planar crystal growth in 2D at a metal electrode.^[21] On the basis of the findings in reference 6, we hypothesize further that if the approach allows both reshaping of undesired crystal growth structures and regulation of the crystal growth orientation, it will not only lead to better morphological control but should enable higher levels of reversibility of the plating and stripping processes during charge and discharge of the electrode.

2. Results and Discussion

To evaluate our hypotheses, we use Zn in the aqueous electrolyte as a model metallic anode system for in-depth study. There is a variety of consideration for selecting Zn for the study; the most important include: i) Zn anodes in neutral aqueous electrolytes do not form complicated solid–electrolyte interphase layers.^[6,12,21,22] The presence of such layers would complicate adsorption processes at the electrode and we believe reduce the fidelity with which polymer, salt, and other known crystal growth-regulation agents are able to regulate crystal growth process at a Zn anode. ii) Our prior success regulating Zn crystallization in the Zn-graphene system^[6] confirms the importance of consideration (i). We note, however, that because the crystal growth regulation is produced by additives in the electrolyte bulk, unlike the Zn-graphene system which relies on

homoepitaxial Zn growth to preserve crystal structures formed at the Zn/graphene interface, the method is simultaneously simpler, easier to scale-up, and is in principle suitable for much higher electrode capacities than possible with any epitaxial regulation strategy. iii) Aqueous rechargeable Zn-ion batteries (ZIB) in which liquid water is the electrolyte solvent offers a large number of practical advantages in terms of low-cost, high safety, ease of scaling-up results from small-scale coin-cell studies to larger format batteries, and rich Zn resources in regions all over the world. Taken together these benefits position ZIBs as a plausible alternative energy storage platform to Lithium-ion batteries, particularly in situations where very large-scale and low-cost electrical energy storage is needed.^[23–25] iv) Zinc's elastic modulus is approximately 20-times higher than that of Li. It means that the consequences of poor morphological (e.g., non-planar deposition, metal orphaning, and short-circuits) are likely to be substantially greater than the corresponding Li case. This underscores the need for easy proliferation of Zn branch dendrite stresses the importance to find an effective method to stabilize the Zn deposition.^[26,27]

To obtain smooth and compact zinc electrodeposition, we propose a crystal growth stabilization method that inhibits growth of the (002) plane of the hexagonal closest packed Zn. This requires a strong inhibitor that shows highly selective preferential absorption at (002) plane, long-lasting activity, and possibility for resupply from the electrolyte bulk. As already noted, this approach offers multiple advantages over the already powerful Zn epitaxial crystal growth strategy reported in our earlier study.^[6] The most important in the present situation is the versatility in interrogating additives with widely varying adsorption characteristics and the ability to regulate the crystal growth from the electrolyte bulk. Meaning that crystal growth structure and orientation can, at least in principle, be regulated in each layer, which makes the method more easily applicable in practical batteries with high areal capacity of Zn anode. This feature is in reality far more important in ZIBs than in studies of lithium anode batteries because the low discharge voltage of ZIB compared to lithium batteries,^[28] makes low capacity Zn anodes less competitive from a practical point of view.

Figure 1 reports the effect of salts and polymer additives on the orientation and morphology of Zn at planar electrodes. The results suggest that halide ions introduce opposite influences in hydrothermal synthesis^[18] and electrodeposition of Zn (Figure 1C–F). In hydrothermal synthesis, chemisorption of halide ions has been reported to lead to highly tunable and oriented crystal growth, while they are seen to cause rough and unregulated crystal growth in Zn electrodeposition (Figure S7–S10, Supporting Information). The scanning electron microscope (SEM) images show that, hexagonal platelet electrodeposits form in ZnSO₄ electrolytes (Figure 1C), whereas a thin scaffold consisting of inner unit sphere-like features form in aqueous ZnX₂ (X = Cl, Br, I) electrolytes (Figure 1D–F). In hydrothermal synthesis chloride ions are reported to be highly effective in inhibiting growth at crystal planed where strong and specific chemisorption occurs.^[29] Based on the Wulff plot for Zn^[10] (Figure S6, Supporting Information), we expect this adsorption to be preferentially at the (002) facets for Zn. The poor ability of any of the Zn salts to promote ordered crystal growth raises obvious questions about the strength and

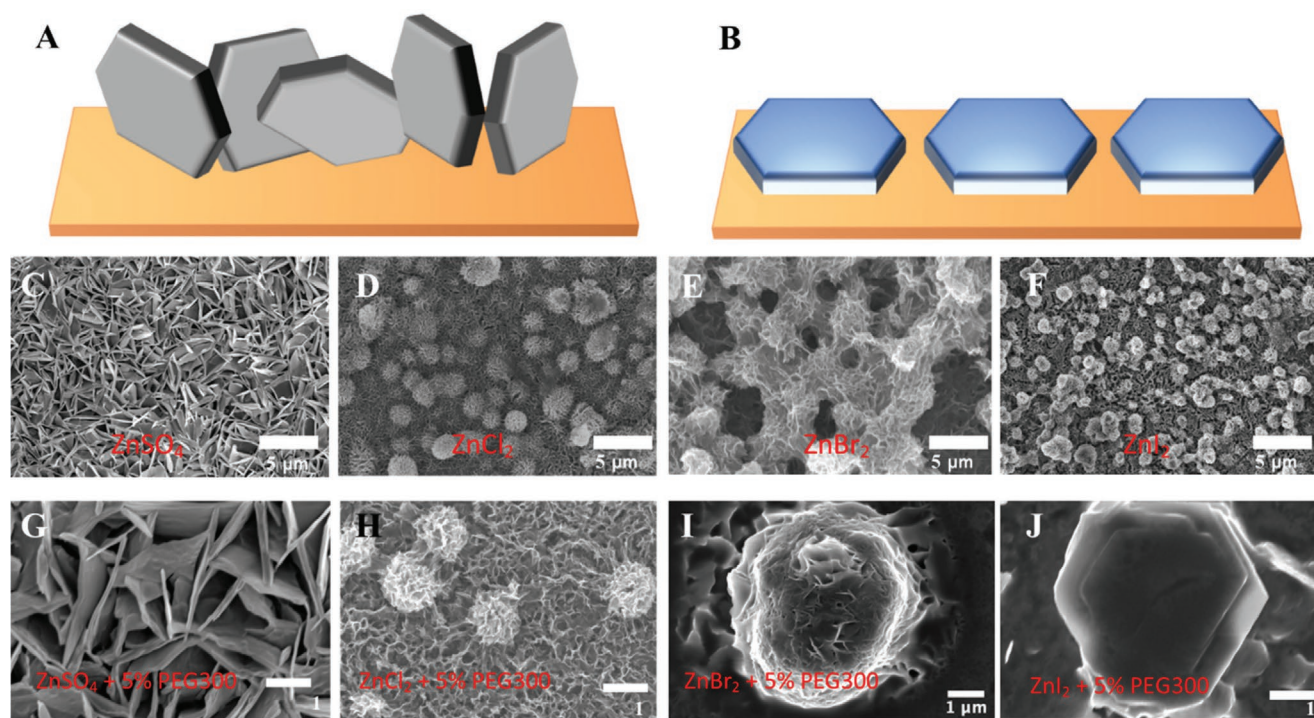


Figure 1. Electrochemical crystal growth of Zn in different electrolytes. Scheme illustrating the Zn crystal growth processes hypothesized A) in ZnSO_4 electrolytes and B) in ZnX_2 + oligomeric polyethylene glycol (PEG 300 g/mol \rightarrow PEG300) electrolytes. Here X = Cl, Br, I is a halogen species. C, G) SEM is used to reveal hexagonal platelet structures formed by electroreduction of Zn from 2 M ZnSO_4 and 2 M ZnSO_4 + 5% PEG300 electrolytes. D–F) Sphere-like structure formed in 2 M ZnCl_2 , ZnBr_2 , and ZnI_2 electrolyte, respectively revealed by SEM analysis. H) Sphere-like structure formed in 2 M ZnCl_2 + 5 wt% PEG300 electrolyte. I) Oval-like structure formed in 2 M ZnBr_2 + 5 wt% PEG300 electrolyte revealed by SEM analysis. J) SEM analysis reveals that large hexagonal platelets are formed by electroreduction of Zn from 2 M ZnI_2 + 5 wt% PEG300 electrolytes.

longevity of the halide ion adsorption at the potentials where Zn electroreduction occurs.

To diagnose the underlying problems of Zinc halide electrolytes, we performed electrochemical impedance spectroscopy (EIS) analysis to characterize the interfacial properties of these electrolytes on the Zn plate surface. As shown in **Figure 2A**, the Nyquist plots of ZnSO_4 and ZnCl_2 show a single semicircle shape, whereas a mass transport region appears in ZnBr_2 and ZnI_2 electrolyte. Significantly, compared with the interfacial resistance of ZnSO_4 and ZnCl_2 electrolytes (158 and 161 Ω), ZnBr_2 and ZnI_2 exhibit remarkably small interfacial resistance, 1.1 and 1.8 Ω , respectively. Considering the minor change in ion conductivity (Figure 2F), we hypothesize that the lowest interfacial resistance of ZnBr_2 and ZnI_2 results from different ion-solvation environment and the strong interfacial ion complexes adsorption on the Zn plate surface. According to previous reports, in the three Zn halide electrolytes studied here, different initial complexes dominate the ionic states due to the electronegativity difference. In ZnCl_2 , stable hexagonal six-coordination complex^[30] $[\text{ZnCl}_4(\text{H}_2\text{O})_2]^{2-}$ predominate the complexes states. In the case of the ZnBr_2 ^[31] and ZnI_2 ^[32] electrolyte, in addition to the stable complexes $[\text{ZnX}_4]^{2-}$ (X = Br, I), unstable complexes $[\text{ZnX}_3]^-$, $[\text{ZnX}_2]$, and $[\text{ZnX}]^+$ (X = Br, I) are also present in large proportions. In ZnSO_4 electrolytes, Zn solvation ions, $[\text{Zn}(\text{H}_2\text{O})_6]^{2+}$ separately exist with SO_4^{2-} . Taken together all these works, the minimal interfacial resistance in ZnBr_2 and ZnI_2 electrolytes is therefore concluded to

be consequences of the interfacial specific adsorption of the unstable complexes $[\text{ZnX}_3]^-$, $[\text{ZnX}_2]$, and $[\text{ZnX}]^+$ (X = Br, I).

To confirm the interfacial specific ion complexes adsorption process, limiting current, which can well reflect the ion transportation properties, at different concentrations was obtained. At low concentration (0.05 M) of these four Zn salts electrolytes (Figure 2G), the limiting currents are close to each other due to the concentration of the unstable ion complexes is low, meaning the interfacial ion complexes adsorption is not strong enough; at higher concentration electrolytes (0.5 M) (Figure 2H), owing to the concentration of unstable ion complexes highly increases and varies in each electrolyte, ZnI_2 electrolyte shows the highest limiting current and an obvious increasing trend was found from ZnSO_4 to ZnI_2 electrolytes. At high concentration electrolytes (1 M) (Figure S2, Supporting Information), Zn halide salts show higher limiting current than ZnSO_4 electrolytes, proving that the interfacial unstable ion-complexes adsorption should be the main reason results in the low interfacial resistance. Exchange current is another powerful parameter to confirm the interfacial unstable ion complexes adsorption. It is shown in Figure 2I that the exchange current of Zn halide salts (i.e., 10^0 mA cm^{-2}) is one order of magnitude higher than that of ZnSO_4 electrolyte (i.e., 10^{-1} mA cm^{-2}), indicating that these unstable ion complexes have much lower de-solvation energy than Zn solvation ion $[\text{Zn}(\text{H}_2\text{O})_6]^{2+}$. Polarization experiments are also in accordance with the exchange current results. 20 mV polarization voltage was used

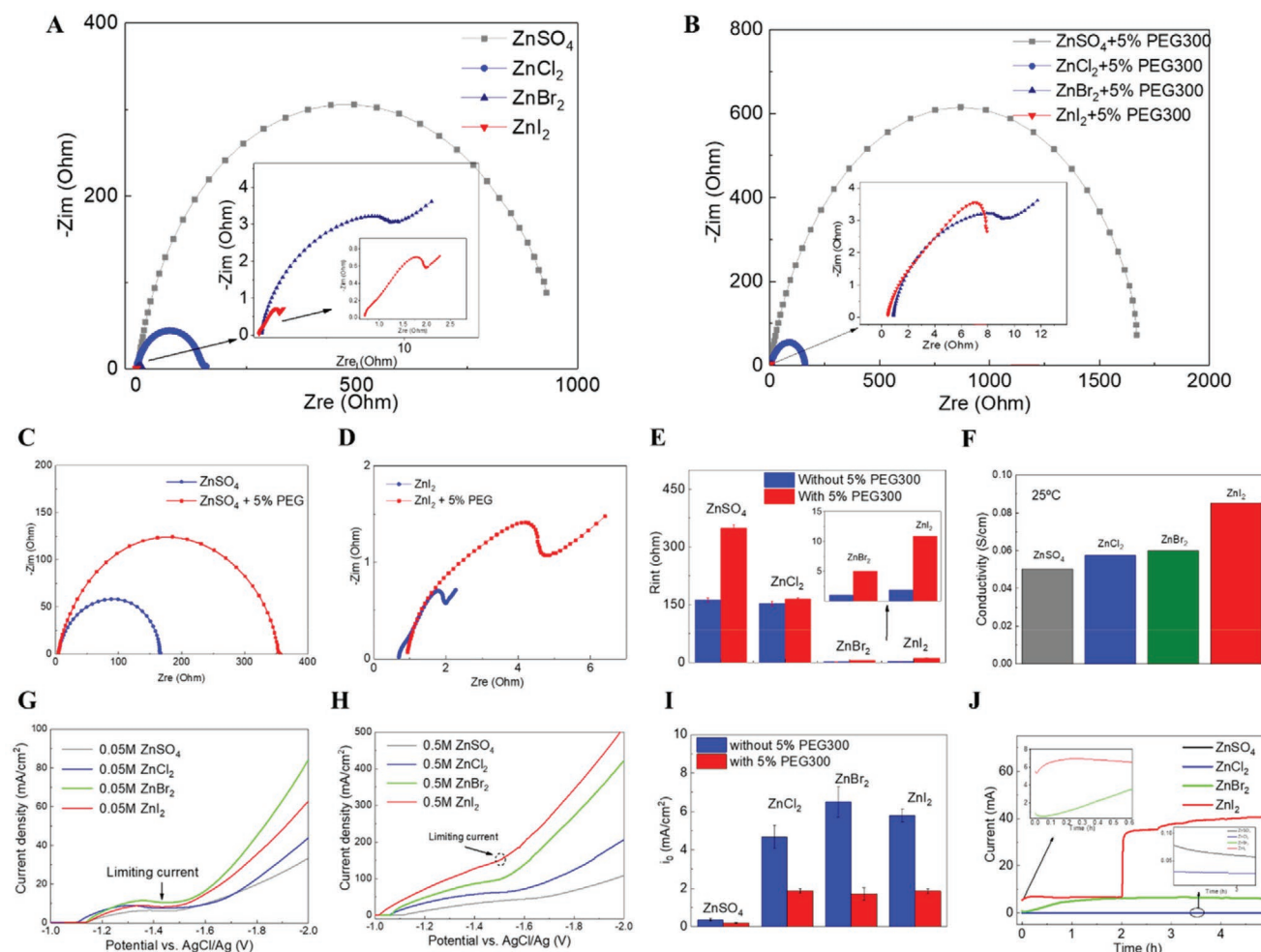


Figure 2. Electrochemical characteristics of ZnSO_4 and ZnX_2 ($\text{X} = \text{Cl}, \text{Br}, \text{I}$) aqueous electrolytes. EIS analysis of A) 2 M ZnSO_4 and various ZnX_2 aqueous electrolytes. B) Same as (A) except containing a fixed concentration (5 wt%) PEG300. C,D) EIS analysis of 2 M ZnSO_4 and ZnI_2 with/without (5 wt%) PEG300. E) Interfacial resistance (R_{int}) calculating by fitting the data in (A,B). F) Ion conductivity calculating from (A). Linear sweep voltammetry of current–voltage curve of ZnSO_4 and various ZnX_2 aqueous electrolytes G) 0.05 M, H) 0.5 M. The plateau or turning points indicate the value of the limiting current. I) Exchange current (i_0) of 2 M ZnSO_4 and ZnX_2 aqueous electrolytes calculated from Tafel plots. J) Current–time curve: 20 mV polarization experiments of 2 M ZnSO_4 and ZnX_2 aqueous electrolytes for 5 h.

to polarize the Zn symmetric cell for 5 h. For ZnSO_4 and ZnCl_2 electrolytes (Figure 2J), the current density is at the microampere level, and the transfer number can be obtained, 0.31 and 0.275, respectively. However, for ZnBr_2 and ZnI_2 electrolytes, Zn electrodeposition occurs at such low polarization voltage, as we clearly observed: 1) the current density is at the milliamper level; 2) as Figure 2J inset shows, the sand's time points were observed; 3) for ZnI_2 electrolytes, the obvious breakpoint indicates the short circuit of the symmetric cell. These results confirm that the unstable ion complex adsorption highly influences the interfacial properties, further affect the crystal growth structure and electrodeposition morphology. Selective crystal growth mentioned above shows that strong interfacial halide adsorption will lead to the different growth rates of different crystal planes. For the halide ion preferred adsorption plane, the growth rate will be greatly affected and then lead to unexpected crystal structure. Here, SEM images shown in Figure 1 reveal that the adsorbed ion complex did distort the crystal structure

from hexagonal platelet to sphere-like structure and lead to unstable reversible electrodeposition (Figure 5), which should result from the specific unstable ion complexes adsorption to certain crystal plane. However, it is known in the literature that multi-valent halide salts form complexes with ether polymers in aqueous solutions.^[33–36] We hypothesized that by tuning the molecular weight of the polymer and composition of these complexes, it should be possible to produce long-lived adsorption and, via the halide ion component, target the adsorption to the (002) Zn crystal facets.

To evaluate this concept, a screening framework was developed to evaluate promising materials as follows: 1) the material should bond with $[\text{ZnX}_3]^-$, $[\text{ZnX}_2]$, and $[\text{ZnX}]^+$ ion complexes, enabling fast and preferential adsorption to the (002) plane of Zn;^[37] 2) the adsorbed material should selectively inhibit growth at the (0002) crystal plane by regulating the ion flux;^[38,39] 3) the material should be nonconductive and charge-free; 4) it should also easily dissolve in the aqueous electrolyte and have limited

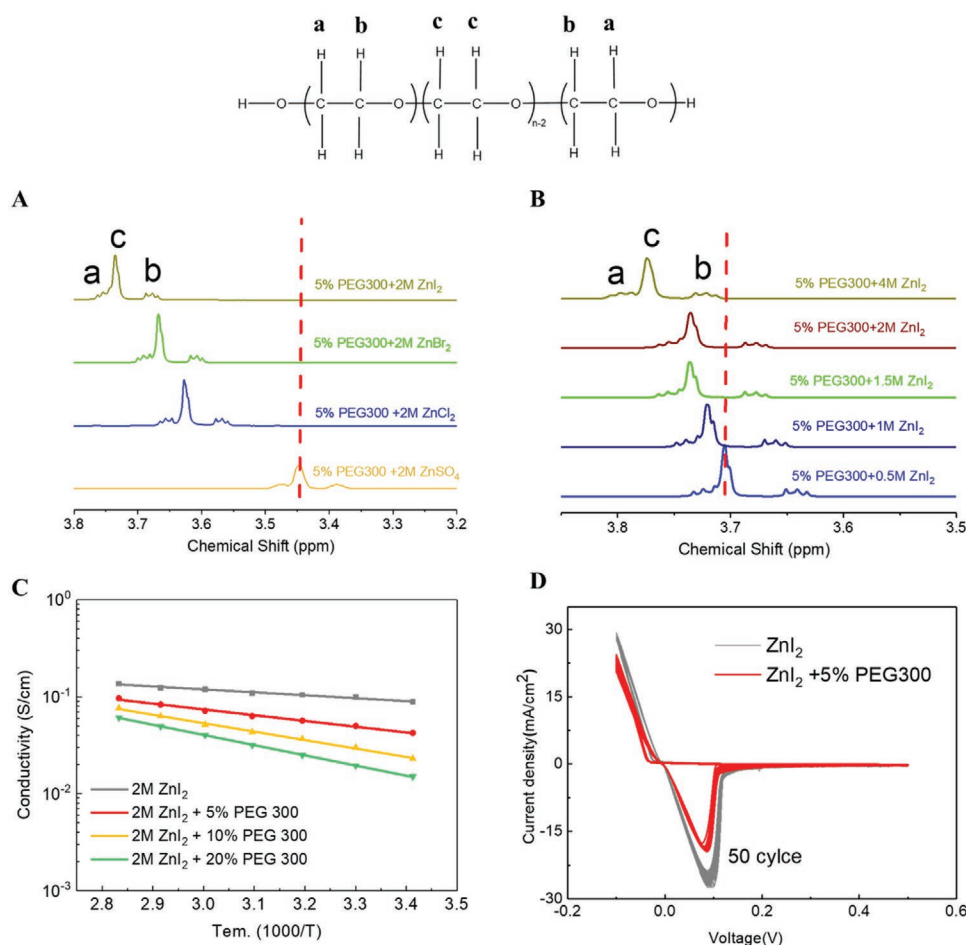


Figure 3. Characteristics of ZnSO_4 and ZnX_2 ($\text{X} = \text{Cl}, \text{Br}, \text{I}$) aqueous electrolytes containing oligomeric polyethylene glycol (PEG 300 g mol $^{-1}$) as a soluble additive. ^1H NMR analysis of A) Various 2 M ZnX_2 aqueous electrolytes containing a fixed concentration (5 wt%) PEG300. B) Same as (A) except the concentration of ZnI_2 in the electrolytes is varied while that of PEG300 is kept fixed at 5 wt%. C) Ion conductivity of 2 M ZnI_2 and ZnI_2 + PEG300 electrolytes. D) CV for the first 50 cycles in a 2 M ZnI_2 and ZnI_2 + 5 wt% PEG300 electrolyte recorded at a fixed scan rate of 10 mV s $^{-1}$.

influence on ion transport features and electrochemical stability of the electrolyte. And, finally, considering the ultimate application value, the material should also be, 5) inexpensive. Within this screening framework, Polyethylene glycol with a molecular weight of 300 g mol $^{-1}$ (PEG300) was singled out as a promising candidate material that meets all the specified criteria.^[37,40,41]

Nuclear Magnetic Resonance (NMR) was used to first understand the initial complexes formed in aqueous electrolytes containing Zn salts with PEG300. It is known that the de-shielding effect results in the right shift of ^1H peak in NMR spectra, therefore, the ^1H peak in the PEG backbone reflects the complexes stability of PEG300, Zn^{2+} , and halide ions. Compared with the PEG ^1H peak in 5%PEG300 + 2 M ZnSO_4 electrolyte, 5% PEG300 + 2 M ZnI_2 shows the strongest de-shielding effect (Shift to the far left), meaning that the PEG readily forms complexes PEG300- $\text{Zn}^{2+}\text{-aI}^-$ ($a = 1, 2, 3$) with the unstable initial complexes $[\text{ZnI}_3]^-$, $[\text{ZnI}_2]$, and $[\text{ZnI}]^+$ (Figure S1B, Supporting Information). Additionally, in Figure 3B, ^1H NMR spectra also show that the de-shielding effect is enhanced as the concentration of ZnI_2 increases, further supporting the idea that a greater $[\text{ZnI}_3]^-$ enhances formation of the PEG- $\text{Zn}^{2+}\text{-aI}^-$ ($a = 1, 2, 3$) complex. EIS analysis (Figure 2C–E and Figure S1, Supporting Information)

shows that the interfacial resistance greatly increases in ZnSO_4 electrolyte, while only minor increases in Zn halide electrolyte, indicating that unlike pure oligomer adsorption process in ZnSO_4 electrolyte, the ion-oligomer complex adsorption happens in Zn halide + PEG300 electrolytes, and is as strong as pure ion complexes adsorption. The decrease of exchange current with PEG300 additives (Figure 2I), also revealed that the ion-oligomer complexes are more stable than pure ion complexes but still possess lower de-solvation energy than Zn solvation ion $[\text{Zn}(\text{H}_2\text{O})_6]^{2+}$.^[2] On this basis, we firstly choose 2 M ZnI_2 + 5 wt% PEG300 electrolytes as the most promising complex for in-depth studies. Conductivity measurements (Figure 3C) indicate that a high concentration of polymer complexes in solution has a negative impact on bulk ion diffusion. Cyclic voltammetry (CV) results also demonstrate that 5 wt% PEG300 has no negative effect on the Zn stripping/plating efficiency and reaction kinetics (Figure 3D). In addition, this low concentration of short-chain PEG has a negligible influence on the electrolyte viscosity (e.g., the viscosity of the electrolyte with and without 5 wt% PEG300 was measured to be 3.202 and 2.819 mPas using a ViscoQC 300).

Figure 4 reports the main result of the present study. The Zn crystal growth morphology in ZnI_2 aqueous electrolyte,

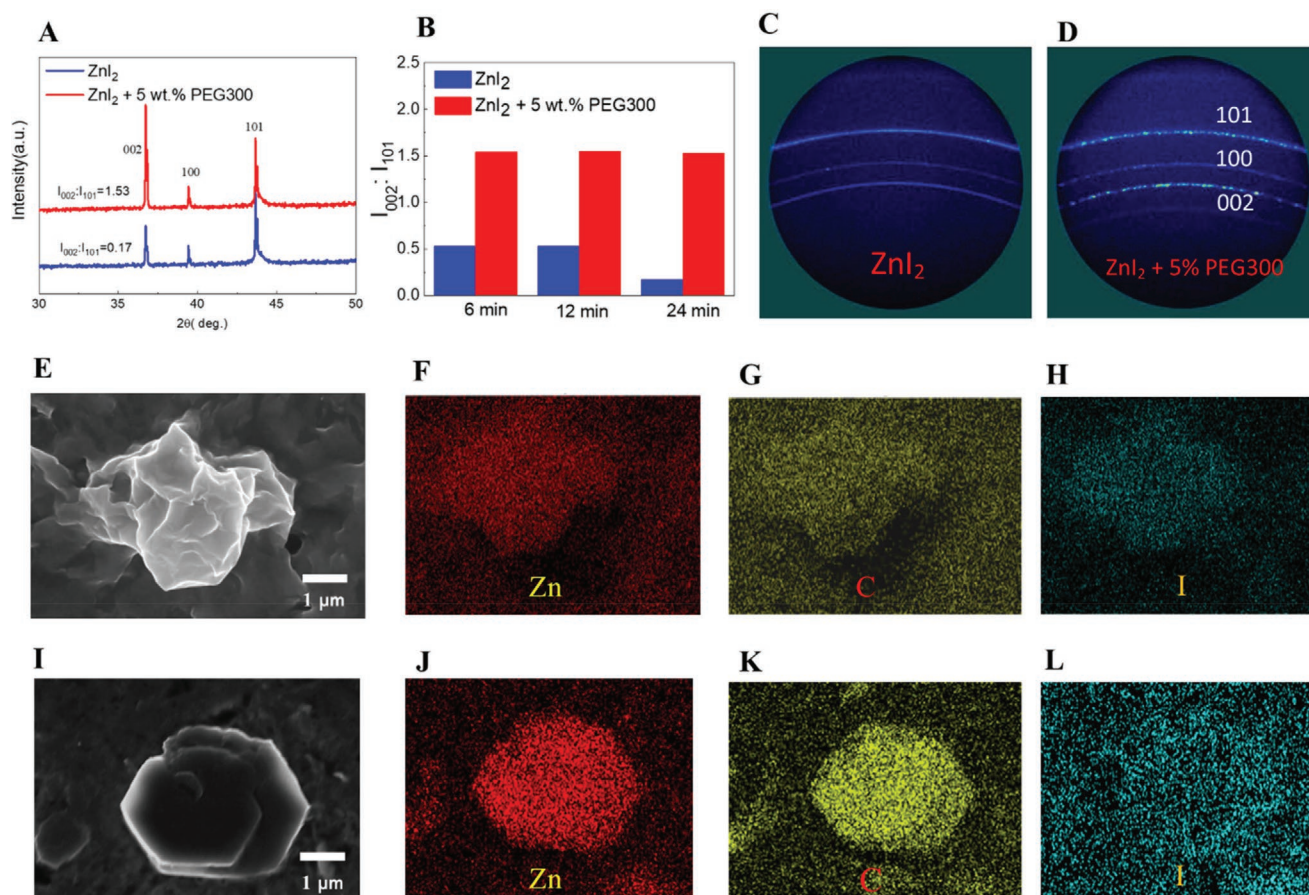


Figure 4. Electrochemical crystal growth structure and orientation of electro-reduced Zn in 2 M ZnI₂ and ZnI₂ + 5 wt% PEG300 aqueous electrolytes. A) XRD analysis of Zn deposits after 24 min growth under galvanostatic conditions at a rate of 4 mA cm⁻². B) The I₀₀₂:I₁₀₁ peak ratio deduced from XRD measurements for Zn deposit after 6, 12, and 24 min growth, again at a fixed rate of 4 mA cm⁻². C,D) 2D grazing incident XRD profiles for Zn deposits formed after 24 min growth in 2 M ZnI₂ and ZnI₂+5 wt% PEG300 electrolyte, respectively, at 4 mA cm⁻². Crystal growth structure in ZnI₂ + 5 wt% PEG300 electrolyte for deposition at E) 40 s, I) 2 min. The corresponding Energy dispersive spectroscopy (EDS) of F,J) Zn, G,K) carbon, and H,I) Iodine.

with/without PEG300 is investigated using SEM, and planar stainless steel is the deposition substrate. As already noted, in pure ZnI₂ electrolyte, the Zn crystal growth shows the sphere-like structure, which grows larger as deposition time increases, ultimately producing unregulated morphologies loosely termed Zn dendrites,^[16] which are easily orphaned upon cycling,^[14] as shown in Figure S7–S10, Supporting Information. In stark contrast to the Zn deposited in the ZnI₂ electrolyte, 2D hexagonal platelet structures are observed 5 wt% PEG300 in ZnI₂ system (Figure 1J). These results are thought to reflect the adsorption control provided by PEG300, which is consistent with our expected crystal growth pattern (Figure 1B). To develop a more in-depth understanding of the crystal growth process, crystal structures at different nucleation times are shown in Figure 4E,I and Figure S4, Supporting Information. The results indicate that the initial crystal growth is consistent with the hypothesis (Figure 1B) and that preferential growth is favored along the 2D substrate plane direction and preferentially exposes the (002) plane of Zn, which is confirmed by the nucleation density result (Figure S11, Supporting Information). To better evaluate changes in the nucleation density induced by the electrolyte additives, we select large scale (1.2 mm)

high-contrast images (Figure S11, Supporting Information) at different nucleation time points: 1 and 1.5 min, $J = 4 \text{ mA cm}^{-2}$. The much higher nucleation density observed in the ZnI₂ + 5 wt% PEG300 electrolyte system indicates that the nucleation rate along the 2D direction is much faster than in ZnI₂ electrolyte, which is again consistent with the idea that Zn crystals prefer to expose the (002) plane because of the slow growth rate of the (002) plane.^[42]

Combining the results of XRD and EDS analysis, we tentatively conclude that PEG300 is preferentially adsorbed to the (002) plane due to the preferential chemisorption of iodide ion (Figure 4H,L). At different nucleation time points, the elements of iodine and carbon (carbon represents the PEG300) are observed to be uniformly distributed at high density on the exposed plane parallel to the substrate (Figure 4G,K). We note that all samples used for these studies were thoroughly washed by Deionized (DI) water for 30 s to remove the residual salt; the fact that the iodine and carbon signal is still obvious, signifying that the preferential adsorption process is very stable. This can be contrasted with the case where the PEG300 is not used (see Figure S12, Supporting Information), where washing lowers the iodine count by 50%. X-ray photoelectron spectroscopy

(XPS) and Quartz Crystal Microbalance (QCM) were used to provide more insight into the adsorption kinetics and to assess the role of PEG300. Zn symmetric cell cycles in 2 M ZnI_2 and $\text{ZnI}_2 + 5 \text{ wt\% PEG300}$ electrolytes for 50 cycles (25 mA cm^{-2} , 3.2 mAh cm^{-2}). After cycling and washing with DI water, XPS analysis of the Zn foil shows obvious Zn 2p and I 3d peaks in the ZnI_2 electrolyte (Figure S13A, Supporting Information), whereas there are no Zn 2p and I 3d peak in the $\text{ZnI}_2 + 5 \text{ wt\% PEG300}$ electrolyte (Figure S13B, Supporting Information), revealing that the adsorbed PEG300 covers the Zn foil and likely exceeds the sensitive thickness (10 nm) of XPS. This latter conclusion is supported by QCM adsorption results. Specifically, the QCM results (Figure S14, Supporting Information) show that on flowing $\text{ZnI}_2 + 5 \text{ wt\% PEG300}$ electrolyte, both the frequency and dissipation values manifest significant shifts (Figure S14A, Supporting Information). Furthermore, we note that the shift in different harmonics do not overlap and the dissipation values are high ($>1 \times 10^{-6}$), indicating that the polymer layer adsorbed on the surface is viscoelastic in nature and cannot be assumed to be a rigid layer. We employed the Voigt viscoelastic model to analyze the 3rd, 5th, and 7th harmonics, revealing that the adsorbed layer has a thickness of approximately 150 nm (Figure S14B, Supporting Information). The QCM results also reveal that the adsorption is reversible, both the frequency and dissipation values plummet to zero when the flowing fluid is switched to buffer solution (2 M ZnI_2), not containing polymer.

To more thoroughly investigate the influence of the electrolyte additives on late-stage Zn deposition morphology, we increase the deposition time. As shown in Figure S9–S10, Supporting Information, the 2D crystal growth pattern shows a much smoother, compacter deposition morphology in $\text{ZnI}_2 + 5 \text{ wt\% PEG300}$ electrolyte compared to the uneven deposition morphology in ZnI_2 electrolyte, which can further be explained by X-ray diffraction (XRD). The peak intensity ratio between I_{002} and I_{101} of the XRD pattern reflects the crystal texturing behavior.^[21] A larger $I_{002}:I_{101}$ means deposits are more (002) texturing, which is parallel to the substrate, meaning smooth and compact deposition. As shown in Figure 4A–D and Figure S15, Supporting Information, the $I_{002}:I_{101}$ is larger and more stable in $\text{ZnI}_2 + 5 \text{ wt\% PEG300}$ electrolyte than in ZnI_2 electrolyte at different deposition time points, meaning the Zn electrodeposition morphology are highly (002) plane orientation under the influence of adsorption PEG300. Taken together our observations, therefore, suggest that we can successfully reshape the crystal structure and further regulate the crystal electrodeposition orientation. The crystal structure has a decisive influence in the deposition morphology, which will greatly affect the cycle life of Zn anode.

To evaluate the reversibility of Zn deposited at high areal capacity, we measured the electrochemical cycling performance of Zn anodes in Zn symmetric cell and plating/stripping CE of Zn deposits in Zn /carbon matrix half-cell. Figure 5A–C shows the galvanostatic cycle curves of Zn/Zn symmetric battery at various current densities and areal capacity. Compared with ZnI_2 electrolyte, $\text{ZnI}_2 + 5 \text{ wt\% PEG300}$ electrolyte shows a better cycle performance due to the 2D hexagonal crystal growth structure and high (002) plane orientation deposition. It is worth noting that the highest area capacity of 15 mAh cm^{-2} and

a cycle time of 630 h were achieved for the first time^[43–48] on a Zn anode with a current density of 15 mA cm^{-2} (Figure 5B). Furthermore, at a current density of 25 mA cm^{-2} , the cycle time with the areal capacity of 3.2 mAh cm^{-2} is over 4000 cycles and 1200 h, which is the longest cycle time at such high current density and areal capacity till now (Figure 5A). Even under the unprecedented high area capacity of 20 mAh cm^{-2} in coin cell, the Zn anode can still work stably over 200 h (Figure 5C). In $\text{ZnI}_2 + 5 \text{ wt\% PEG300}$ electrolyte, the Zn foil after 1000 cycles (25 mA cm^{-2} and 3.2 mAh cm^{-2}) shows the uniform plating/stripping morphology compared to the dendritic surface of Zn foil in the ZnI_2 electrolyte after short circuit (50 cycles) (Figure S16, Supporting Information). On the other hand, the CE, which reveals the ratio between the plating and stripping metal in each cycle, also indicates the better electrodeposition performance of $\text{ZnI}_2 + 5 \text{ wt\% PEG300}$ electrolyte. Considering that the limitation of planar stainless steel at high areal capacity, we choose 3D interwoven carbon fibers (carbon matrix) as a deposition substrate which can supply a high deposition area. In stark contrast to the rapid battery failure observed in ZnI_2 electrolyte (Figure 5D), $\text{ZnI}_2 + 5 \text{ wt\% PEG300}$ electrolyte manifests a high level of reversibility (99.1–99.8%) at high areal capacity of 3.2 mAh cm^{-2} (Figure 5D). The voltage profile confirms that the plating/stripping reaction is stable (Figure 5E).

The final important consideration is that since the successful crystal growth control with PEG300 in ZnI_2 electrolyte, will it work in ZnBr_2 and ZnCl_2 electrolyte? We found that PEG300 can partially control the crystal growth in $\text{ZnBr}_2 + 5 \text{ wt\% PEG300}$ electrolyte. As shown in Figure 1I, compared with the sphere-like structure, complete large oval structures with a planar plane facing us can be observed. However, the crystal growth pattern is more complicated in $\text{ZnCl}_2 + 5 \text{ wt\% PEG300}$ electrolyte. At the initial deposition period, we observe two kinds of structures: sphere-like and hexagonal platelet structures (Figure S18, Supporting Information). As deposition time increases, only sphere-like structures are observed (Figure 1H). Hence, we think that PEG300 fails to reshape the crystal growth structure in $\text{ZnCl}_2 + 5 \text{ wt\% PEG300}$ electrolyte. Cycling performance of the Zn symmetric cell is consistent with the control result of crystal growth structure (Figure S19, Supporting Information). The best crystal growth control, the hexagonal platelet structure, in $\text{ZnI}_2 + 5 \text{ wt\% PEG300}$ electrolyte shows the longest cycle time, whereas the failure of crystal control in $\text{ZnCl}_2 + 5 \text{ wt\% PEG300}$ electrolyte shows the shortest cycle time. Two considerations are taken into account to the greatly different crystal growth structures in ZnX_2 ($\text{X} = \text{Cl}, \text{Br}, \text{I}$) + 5 wt% PEG300 electrolytes: 1) as ^1H NMR spectra analysis shows, due to the high concentration of unstable complexes $[\text{ZnI}_3]^-$ in ZnI_2 electrolyte, the energy barrier of forming $\text{PEG300-Zn}^{2+}\cdot\text{aI}^-$ ($\text{a} = 1, 2, 3$) complex is lower, which has an indispensable influence in the adsorption process as we think it's halide's preferential adsorption that effects the PEG300 adsorption.^[39] 2) Under high current density, compared with chloride and bromide, iodide has a strong chemisorption ability to the gold (111) electrode surface due to the covalent bond character between adsorbed iodide and metal surface.^[49] Correspondingly, we believe that iodide also has the strongest preferential chemisorption ability to the (002) crystal plane of Zn, which highly enhances the control ability

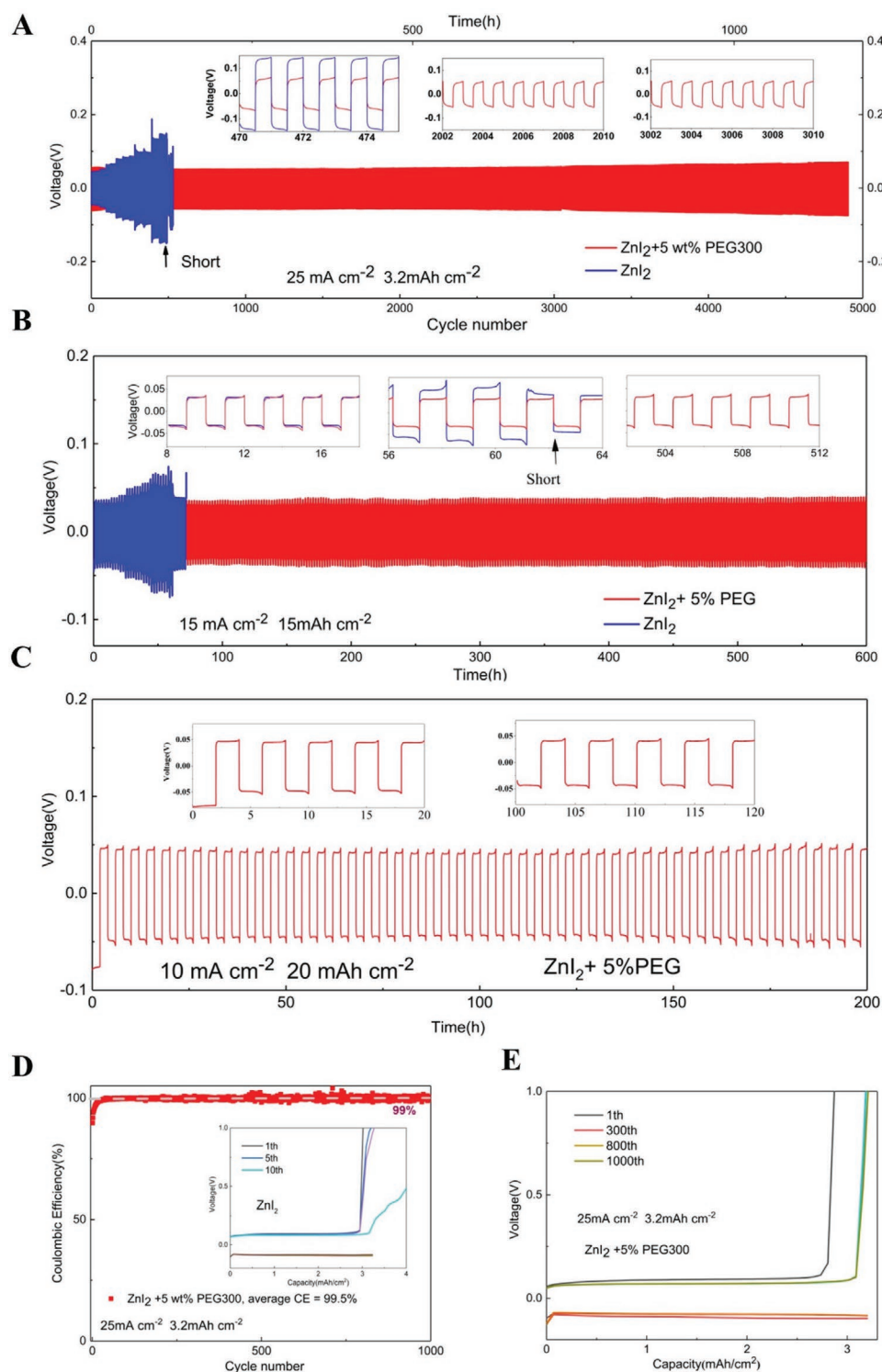


Figure 5. Galvanostatic cycling behavior of Zn anodes in 2 M ZnI₂ and ZnI₂ + 5 wt% PEG300 aqueous electrolytes. Cycling performance of Zn||Zn symmetric cells at A) 25 mA cm⁻², 3.2 mAh cm⁻². B) 15 mA cm⁻², 15 mAh cm⁻². C) 10 mA cm⁻², 20 mAh cm⁻². D) CE measured in Zn plate-strip experiments in Zn||carbon matrix half-cells in a 2 M ZnI₂ + 5 wt% PEG300 electrolyte. The inset is the voltage–capacity curve for the corresponding Zn||carbon matrix half-cell in which 2 M ZnI₂ is used as the electrolyte for current densities of 25 mA cm⁻² and 3.2 mAh cm⁻². E) The Voltage–areal capacity plot for Zn||carbon matrix half-cell in 2 M ZnI₂ + 5 wt% PEG300 electrolyte at 25 mA cm⁻² and 3.2 mAh cm⁻².

of crystal growth process in ZnI₂ + PEG electrolyte compared with other two Zn halide electrolytes. Furthermore, the poor

cycling performance of Zn symmetric cells in ZnCl₂ + 5 wt% PEG300 and ZnBr₂ + 5 wt% PEG300 electrolytes indicate the

importance of hexagonal platelet crystal growth structure and highly oriented deposition morphology to the Zn anode. On this basis, we conclude that regulating metal electrodeposition morphology by controlling crystal growth structure and orientation is a rational and available method.

Benefiting from the high areal capacity and long cycle time of the Zn anode, we further investigate the performance of Zn/I₂ full batteries in coin cell and flow battery, respectively. In Zn/I₂ coin cell, due to strong adsorption ability to the I₃[−], activated carbon (AC) can be used as cathode materials, which can well reduce the shuttle effect of I₃[−] in the aqueous electrolyte. The Zn||AC full battery shows the stable charge/discharge plateau and different areal capacity at different current densities (Figure S20, Supporting Information). The reaction during charge/discharge should be:

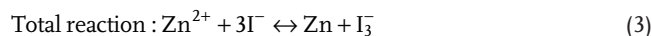


Figure 6A,B reports that the Zn/I₂ coin cell has a high areal capacity of 1 mAh cm^{−2} at a current density of 2 mA cm^{−2}, achieving 1000 cycles without fading. To demonstrate the advantages of the high area capacity Zn anode system and push it to the height of application, the flow battery is a good model to prove our system. We choose the previously reported electrolyte⁵⁰: 6 M KI and 3 M ZnBr₂ and adding 5 wt% PEG300 to the anolyte side. Considering that the iodine deposition will block the flowing tube, we use single-flow battery here.^[50] As Figure 6C,D shows, the Zn/I₂ flow battery has a high areal capacity of 10 mAh cm^{−2} at a current density of 40 mA cm^{−2}, stability running 120 cycles with high CE 99.5%. After 120 cycles,

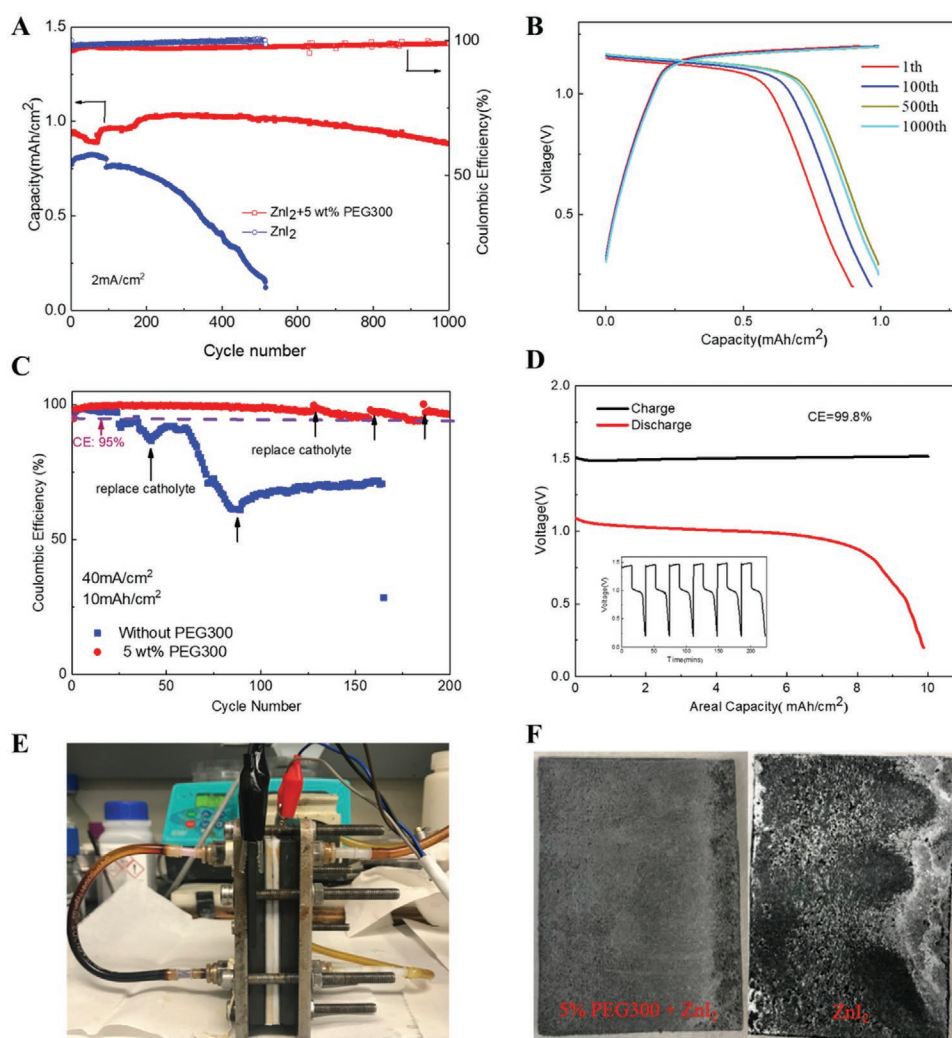


Figure 6. Full Zn||I₂ battery cell performance in 2 M ZnI₂ and ZnI₂ + 5 wt% PEG300 aqueous electrolytes. A) Cycling performance of Zn||I₂ coin cells at 2 mA cm^{−2}. B) Charge/discharge curve of Zn||I₂ coin cell at a current density of 2 mA cm^{−2}. C) CE of Zn||I₂ electrochemical flow battery. D) The Voltage-areal capacity profile in the first few cycles of a 10 mAh cm^{−2} Zn||I₂ flow battery with PEG300 additive at 40 mA cm^{−2}. E) Photograph of the single-flow Zn||I₂ flow cell. F) Deposition morphology of Zn on the carbon felt anode current collector for the Zn||I₂ flow cell after 10 cycles, with/without PEG300.

the CE shows a little drop. However, after we replace the catholyte, the CE recovers to 99.5%, meaning the iodine deposition side is the main problem for our system. We replace the catholyte three times and the flow battery system can work over 200 cycles. On the contrary, the CE keeps dropping after we replace the catholyte in the electrolyte without PEG300. The deposition morphology (Figure 6F) well reflects the smooth deposition in PEG300 additive electrolyte. Owing to the non-dendrite Zn anode with PEG300 additives, theoretically, we can keep the flow battery working for a long time by replacing the catholyte.

3. Conclusion

We report that crystal growth stabilization method, including reshaping the crystal growth structure and regulating the crystal deposition orientation, is a good way to control the metal electrodeposition morphology and further has a great impact on the battery anode cycle performance. Taking Zn anode as a good example, the Zn anode achieves unprecedented cycle performance at the high current density and areal capacity using carefully selected PEG-Zn²⁺-aI⁻ (a = 1,2,3) complexes system to control the crystal growth process. On the contrary, the failure of controlling crystal growth structure indicates the poor cycle performance of Zn anode. We further demonstrate the application value of this electrolyte system in coin cell and a single flow battery, both of which show excellent performance at a high areal capacity. Our findings point out the importance to control crystal growth in the metal anode system. To pursue the high areal capacity metal anodes, which can meet the application requirements, crystal growth structure and orientation are the key steps that must be noticed.

Supporting Information

Supporting Information is available from the Wiley Online Library or from the author.

Acknowledgements

S.J. and D.Z. contributed equally to this work. This work was supported by the Department of Energy Basic Energy Sciences Program through Award DE-SC0016082. Electron microscopy and X-ray diffraction facilities supported by the Cornell Center for Materials Research with funding from the NSF MRSEC program (DMR-1719875) were employed in the study.

Conflict of Interest

The authors declare no conflict of interest.

Data Availability Statement

Research data are not shared.

Keywords

crystallography, electrodeposition, flow batteries, low-cost batteries, polyethylene glycol

Received: April 2, 2021

Revised: April 28, 2021

Published online: July 6, 2021

- [1] Y. Liang, H. Dong, D. Aurbach, Y. Yao, *Nat. Energy* **2020**, 1.
- [2] K. R. Lawless, *J. Vac. Sci. Technol.* **1965**, 2, 24.
- [3] F. Sun, W. P. Cai, Y. Li, B. Cao, F. Lu, G. Duan, L. Zhang, *Adv. Mater.* **2004**, 16, 1116.
- [4] K. K. Gleason, *Nat. Rev. Phys.* **2020**, 2, 347.
- [5] D. Lin, Y. Liu, Y. Cui, *Nat. Nanotechnol.* **2017**, 12, 194.
- [6] J. Zheng, Q. Zhao, T. Tang, J. Yin, C. D. Quilty, G. D. Renderos, X. Liu, Y. Deng, L. Weng, D. C. Bock, C. Jaye, D. Zhang, E. S. Takeuchi, K. J. Takeuchi, A. C. Marschillok, L. A. Archer, *Science* **2019**, 366, 645.
- [7] M. C. Lin, M. Gong, B. Lu, Y. Wu, D.-Y. Wang, M. Guan, M. Angell, C. Chen, J. Yang, B.-J. Hwang, H. Dai, *Nature* **2015**, 520, 324.
- [8] Q. Zhao, M. J. Zachman, W. I. Al Sadat, J. Zheng, L. F. Kourkoutis, L. A. Archer, *Sci. Adv.* **2018**, 4, eaau8131.
- [9] F. Shi, A. Pei, A. Vailionis, V. J. Xie, B. Liu, J. Zhao, Y. Gong, Y. Cui, *Proc. Natl. Acad. Sci. U. S. A.* **2017**, 114, 12138.
- [10] J. Zheng, M. S. Kim, Z. Tu, S. Choudhury, T. Tanga, L. A. Archer, *Chem. Soc. Rev.* **2020**, 49, 2701.
- [11] W. Liu, P. Liu, D. Mitlin, *Chem. Soc. Rev.* **2020**, 49, 7284.
- [12] M. D. Tikekar, S. Choudhury, Z. Tu, L. A. Archer, *Nat. Energy* **2016**, 1, 16114.
- [13] Y. Sawada, A. Dougherty, J. P. Gollub, *Phys. Rev. Lett.* **1986**, 56, 1260.
- [14] J. Zheng, T. Tang, Q. Zhao, X. Liu, Y. Deng, L. A. Archer, *ACS Energy Lett.* **2019**, 4, 1349.
- [15] C. Fang, J. Li, M. Zhang, Y. Zhang, F. Yang, J. Z. Lee, M.-H. Lee, J. Alvarado, M. A. Schroeder, Y. Yang, B. Lu, N. Williams, M. Ceja, L. Yang, M. Cai, J. Gu, K. Xu, X. Wang, Y. S. Meng, *Nature* **2019**, 572, 511.
- [16] S. Higashi, S. W. Lee, J. S. Lee, K. Takeuchi, Y. Cui, *Nat. Commun.* **2016**, 7, 11801.
- [17] Y. Deng, J. Zheng, A. Warren, J. Yin, S. Choudhury, P. Biswal, D. Zhang, L. A. Archer, *Adv. Energy Mater.* **2019**, 9, 1901651.
- [18] S. S. Shankar, S. Bhargava, M. Sastry, *J. Nanosci. Nanotechnol.* **2005**, 5, 1721.
- [19] B. Wiley, T. Herricks, Y. Sun, Y. Xia, *Nano Lett.* **2004**, 4, 1733.
- [20] O. M. Magnussen, B. M. Ocko, R. R. Adzic, J. X. Wang, *Phys. Rev. B: Condens. Matter Mater. Phys.* **1995**, 51, 5510.
- [21] J. Zheng, J. Yin, D. Zhang, G. Li, D. C. Bock, T. Tang, Q. Zhao, X. Liu, A. Warren, Y. Deng, S. Jin, A. C. Marschillok, E. S. Takeuchi, K. J. Takeuchi, C. D. Rahn, L. A. Archer, *Sci. Adv.* **2020**, 6, eaab1122.
- [22] J. Zheng, L. A. Archer, *Sci. Adv.* **2021**, 7, eaab0219.
- [23] C. Zhong, B. Liu, J. Ding, X. Liu, Y. Zhong, Y. Li, C. Sun, X. Han, Y. Deng, N. Zhao, W. Hu, *Nat. Energy* **2020**, 5, 440.
- [24] J. W. Choi, D. Aurbach, *Nat. Rev. Mater.* **2016**, 1, 16013.
- [25] F. Wang, O. Borodin, T. Gao, X. Fan, W. Sun, F. Han, A. Faraone, J. A. Dura, K. Xu, C. Wang, *Nat. Mater.* **2018**, 17, 543.
- [26] M. Biton, F. Tariq, V. Yufit, Z. Chen, N. Brandon, *Acta Mater.* **2017**, 141, 39.
- [27] A. Khor, P. Leung, M. R. Mohamed, C. Floxa, Q. Xu, L. An, R. G. A. Wills, J. R. Morante, A. A. Shah, *Mater. Today Energy* **2018**, 8, 80.
- [28] P. Albertus, S. Babinec, S. Litzelman, A. Newman, *Nat. Energy* **2018**, 3, 16.

- [29] A. Filankembo, M. P. Pileni, *J. Phys. Chem. B* **2000**, *104*, 5865.
- [30] D. E. Irish, B. McCarroll, T. F. R. Young, *J. Chem. Phys.* **1963**, *39*, 3436.
- [31] E. Kálmán, I. Serke, G. Pálkás, G. Johansson, G. Kabisch, M. Maeda, H. Ohtaki, *Zeitschrift für Naturforschung A* **1983**, *38*, 225.
- [32] H. Wakita, G. Johansson, M. Sandström, P. L. Goggin, H. Ohtaki, *J. Solution Chem.* **1991**, *20*, 643.
- [33] L. Bulgariu, D. Bulgariu, *Sep. Sci. Technol.* **2007**, *42*, 1093.
- [34] L. Bulgariu, D. Bulgariu, I. Sârghie, T. Măluțan, *Open Chem.* **2007**, *5*, 291.
- [35] L. Bulgariu, D. Bulgariu, *Sep. Purif. Technol.* **2011**, *80*, 620.
- [36] S. J. Banik, R. Aklolkar, *J. Electrochem. Soc.* **2013**, *160*, D519.
- [37] Z. V. Feng, X. Li, A. A. Gewirth, *J. Phys. Chem. B* **2003**, *107*, 9415.
- [38] T. P. Moffat, J. E. Bonevich, W. H. Huber, A. Stanishevsky, D. R. Kelly, G. R. Stafford, D. Josell, *J. Electrochem. Soc.* **2000**, *147*, 4524.
- [39] K. R. Hebert, *J. Electrochem. Soc.* **2005**, *152*, C283.
- [40] M. Hasegawa, Y. Okinaka, Y. Shacham-Diamand, T. Osaka, *Electrochem. Solid-State Lett.* **2006**, *9*, C138.
- [41] M. Wilms, P. M. Broekmann, Z. P. Kruff, C. Stuhlmann, K. Wandelt, *Surf. Sci.* **1998**, *402*, 83.
- [42] P. Biswal, S. Stalin, A. Kludze, S. Choudhury, L. A. Archer, *Nano Lett.* **2019**, *19*, 8191.
- [43] C. Shen, X. Li, N. Li, K. Xie, J.-g. Wang, X. Liu, B. Wei, *ACS Appl. Mater. Interfaces* **2018**, *10*, 25446.
- [44] K. Zhao, C. Wang, Y. Yu, M. Yan, Q. Wei, P. He, Y. Dong, Z. Zhang, X. Wang, L. Mai, *Adv. Mater. Interfaces* **2018**, *5*, 1800848.
- [45] Q. Zhang, J. Luan, L. Fu, S. Wu, Y. Tang, X. Ji, H. Wang, *Angew. Chem., Int. Ed. Engl.* **2019**, *58*, 15841.
- [46] P. Liang, J. Yi, X. Liu, K. Wu, Z. Wang, J. Cui, Y. Liu, Y. Wang, Y. Xia, J. Zhang, *Adv. Funct. Mater.* **2020**, *30*, 1908528.
- [47] Y. Zeng, X. Zhang, R. Qin, X. Liu, P. Fang, D. Zheng, Y. Tong, X. Lu, *Adv. Mater.* **2019**, *31*, 1903675.
- [48] R. Yuksel, O. Buyukcakil, W. K. Seong, R. S. Ruoff, *Adv. Energy Mater.* **2020**, *10*, 1904215.
- [49] A. Chen, Z. Shi, D. Bizzotto, J. Lipkowski, B. Pettinger, C. Bilger, *J. Electroanal. Chem.* **1999**, *467*, 342.
- [50] C. Xie, Y. Liu, W. Lu, H. Zhang, X. Li, *Energy Environ. Sci.* **2019**, *12*, 1834.